JOURNAL OF AIRCRAFT
Vol. 31, No. 1, Jan.–Feb. 1994

Nonslender Waveriders

X. He* and G. Emanuel†
University of Oklahoma, Norman, Oklahoma 73019

A new body-oriented procedure for generating nonslender waverider shapes is described. These shapes are more practical than conventional waveriders that are relatively slender. Aside from slenderness, the method provides control over the included angle at the leading edge of the waverider, which is structurally important. A new procedure for rounding the leading edge is also presented. Although the lift-to-drag ratio is less for a nonslender waverider, relative to a slender one, it is still quite large. Lift-to-drag is thus traded for improved volumetric effectiveness, thicker winglets, and easier matching with the aft portion of a waverider-based vehicle. By means of hypersonic small-disturbance theory, an on-design parametric study is performed. Off-design performance is provided by solutions of an Euler space-marching code. Both studies verify the feasibility for developing nonslender waveriders.

Nomenclature

A, B = coefficients for freestream curve
A_b = waverider base plane area
b = width of waverider in the base plane
C_D = drag coefficient
$C_{D\,\mathrm{inv}}$ = inviscid drag coefficient
C_f = average skin friction coefficient
C_L = lift coefficient
K_δ = hypersonic similarity parameter, $M_\infty\delta$
L/D = lift-to-drag ratio
l = length of basic cone
l_w = length of waverider
M_∞ = freestream Mach number
$M_{\infty d}$ = design Mach number
R_0 = normalized radial distance to freestream surface in symmetry plane
S_b = shock layer base plane area
S_p = projected planform area
S_w = wetted surface area
t = waverider thickness in the base and symmetry planes
V = volume of waverider
X, Y = normalized Cartesian coordinates in the base plane
X_σ, Y_σ = normalized shock location in the base plane
α = angle of attack
β = shock angle
γ = ratio of specific heats
δ = half cone angle
η = volumetric parameter, $V^{2/3}/S_p$
Λ_b = waverider edge angle in the base plane
Λ_{be} = maximum waverider edge angle in the base plane
Λ_n = waverider edge angle at nose
σ = ratio of shock angle to cone angle
τ = thickness ratio
ϕ_l = anhedral angle
Ω_∞ = slope angle of freestream surface at edge in the base plane
ω_Λ = edge angle parameter
ω_τ = volume distribution parameter

Introduction

WAVERIDER-BASED vehicles are of interest for supersonic and hypersonic flight since they provide a large L/D. In 1990, the First International Hypersonic Waverider Symposium was devoted to this technology. Since the symposium, additional publications have appeared.[1-5] A common element of the analysis in these publications is that waveriders are typically viewed as slender vehicles. This has led to difficulties when attempting to mate a waverider forebody with the rest of the vehicle. The aft portion would prefer a thicker forebody, particularly in the base plane of the waverider where they merge. A nonslender waverider would provide better packaging, and a reduction in the skin friction of the forebody. A slender waverider generally possesses a sharp leading edge, which is not realistic, and a thin structure adjacent to the leading edge. This leading edge may not be able to handle the large structural and heat transfer loads. These are important limitations blocking future development of waveriders.

Hypersonic small-disturbance theory (HSDT) is used to establish a new approach for the design of nonslender waveriders. As expected, the wave drag is increased relative to a slender waverider counterpart, and the L/D is less. However, one can show that a high L/D forebody does not imply a large L/D for the integrated vehicle. The overall reduction in L/D is partly offset because the nonslender waverider has less viscous drag compared to that of a slender waverider. The design approach presented here controls the magnitude of the included angle between the freestream and compression surfaces at the leading edge. Along with rounding, this feature overcomes the problems associated with a thin structure near the leading edge.

The object of this work is to develop a generic design approach that yields practical waverider configurations. In this context, we assume an endoatmospheric vehicle and choose its design point to coincide with its maximum anticipated hypersonic flight Mach number, $M_{\infty d}$. At this condition, the vehicle experiences its maximum drag and heat transfer. A major benefit of this approach is that the bow shock is detached when $M_\infty < M_{\infty d}$. This is in contrast to the interaction, downstream of the leading edge, between the shock wave and boundary layer that occurs when $M_\infty > M_{\infty d}$. This interaction can result in boundary-layer separation and a large local heat transfer rate. Other benefits are discussed later. Therefore, when off-design performance is evaluated, M_∞ will not exceed the $M_{\infty d}$ design value.

Received Aug. 25, 1992; revision received Nov. 4, 1992; accepted for publication Nov. 4, 1992. Copyright © 1993 by the American Institute of Aeronautics and Astronautics, Inc. All rights reserved.

*Adjunct Assistant Professor, School of Aerospace and Mechanical Engineering, 865 Asp Ave., Room 212. Member AIAA.
†Professor, School of Aerospace and Mechanical Engineering, 865 Asp Ave., Room 212. Associate Fellow AIAA.

In the next section, the HSDT approach is developed. We also describe the Euler code used to validate the HSDT and to perform off-design calculations. This section concludes with a brief discussion of leading-edge rounding. The next section provides on- and off-design results for geometric and aerodynamic waverider properties. The final section contains a summary of our findings. The dissertation by He[6] should be consulted for additional details that cannot be included here.

Formulation

Hypersonic Small-Disturbance Theory

Inviscid, supersonic flow of a perfect gas is considered about a cone at zero incidence. The coordinate system and much of the nomenclature is shown in Fig. 1. Aside from γ ($=1.4$), the conical flowfield between the shock and cone is governed by δ and M_∞. With the aid of HSDT,[6-8] the shock wave angle is given by

$$\sigma \equiv \frac{\beta}{\delta} = \left[\frac{\gamma+1}{2} + \frac{1}{K_\delta^2}\right]^{1/2} \tag{1}$$

where $K_\delta = M_\infty \delta$. Following Refs. 7 and 8, it is convenient to consider waveriders that have a freestream curve in the base plane determined by an even polynomial

$$X = R_0 + AY^2 + BY^4 \tag{2}$$

where X, Y, and R_0 are normalized using $l\delta$ (Fig. 1). The A and B coefficients are usually found by specifying R_0 and ϕ_l, which are coordinate dependent. A different system of body-oriented parameters, however, will be introduced to expedite the design of nonslender waveriders. A higher degree polynomial, as well as other forms, can be used for Eq. (2). The basic approach is not dependent on the specific representation of the freestream curve.

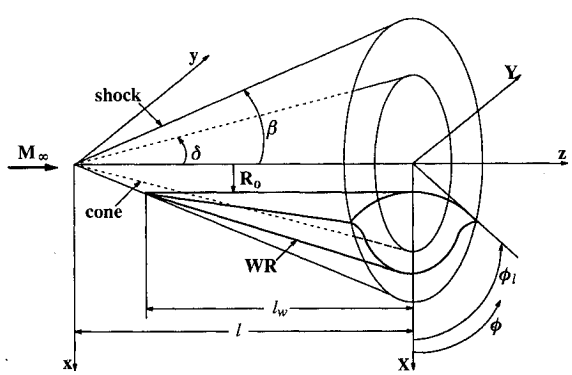

Fig. 1 Construction of a general cone-derived waverider, where the X, Y coordinates are shown in the base plane.

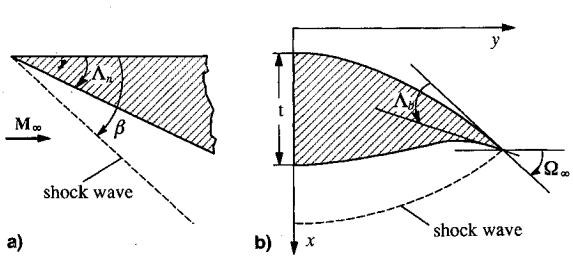

Fig. 2 Schematic showing a) nose angle Λ_n in the symmetry plane and b) t and Λ_b and Ω_∞ in the base plane.

Figure 2 shows the freestream surface angle at the edge in the base plane (Ω_∞). This specified parameter is related to A and B through

$$\tan \Omega_\infty = \left(\frac{dX_\infty}{dY_\infty}\right)_\sigma = (2AY_\infty + 4BY_\infty^3)_\sigma$$

where the σ subscript denotes the leading edge in the base plane, and

$$X_\sigma = \sigma \cos \phi_l, \qquad Y_\sigma = \sigma \sin \phi_l \tag{3}$$

We thus obtain

$$A + 2(\sigma \sin \phi_l)^2 B = \frac{\tan \Omega_\infty}{2\sigma \sin \phi_l} \tag{4}$$

Equations (2) and (3) also yield the leading-edge constraint

$$A + (\sigma \sin \phi_l)^2 B = \frac{\sigma \cos \phi_l - R_0}{(\sigma \sin \phi_l)^2} \tag{5}$$

Figure 2 also shows the edge angle Λ whose exact value at the nose is[8]

$$\Lambda_n = \beta - \tan^{-1}\left[\frac{2 + (\gamma-1)M_\infty^2 \sin^2\beta}{(\gamma+1)M_\infty^2 \sin\beta \cos\beta}\right]$$

When β is small, the HSDT form is

$$M_\infty \Lambda_n \triangleq \frac{K_\delta^2}{[1 + (\gamma+1)K_\delta^2/2]^{1/2}} = \frac{K_\delta}{\sigma}$$

Thus, $M_\infty \Lambda_n$ is determined by K_δ, and does not depend on any of the parameters that define the shape of the waverider. Figure 3 shows $(M_\infty \Lambda_n)/10$ with Λ_n in degrees. (All angles in the figures and table are in degrees.) For a waverider with $M_{\infty d} = 8$ and $\delta = 10$ deg, Λ_n equals 7.5 deg. While this is not a large angle, Λ_n would be only 3.7 deg if $\delta = 6$ deg, a frequently encountered value for δ. Thus, a relatively large value for δ is required for a useful Λ_n value.

By definition, the included edge angle Λ is in a plane normal to the leading edge. The leading edge in the base plane,

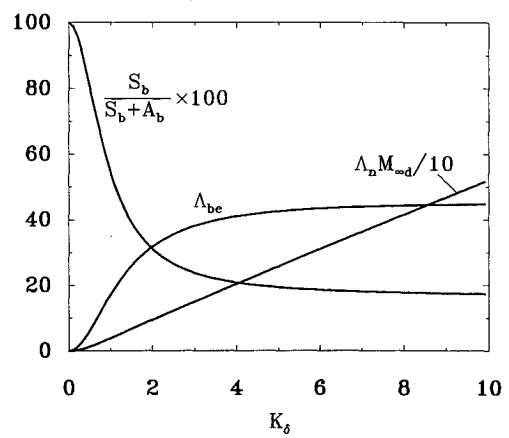

Fig. 3 Angles $(\Lambda_n M_{\infty d})/10$ and Λ_{be}, and the shock layer fractional area as a function of the hypersonic similarity parameter.

however, typically has a sweep angle in excess of 70 deg; we therefore approximately evaluate Λ_b in the base plane as[6]

$$\tan \Lambda_b = \frac{\sin(\Omega_\infty + \phi_l)\cos(\Omega_\infty + \phi_l)}{\sigma^2 - \sin^2(\Omega_\infty + \phi_l)} \tag{6}$$

With σ fixed, Λ_b has a maximum value determined by $\partial\Lambda_b/\partial\Omega_\infty = 0$, or $\partial\Lambda_b/\partial\phi_l = 0$. This yields

$$\Lambda_{be} = \sin^{-1}\left(\frac{1}{2\sigma^2 - 1}\right) = \sin^{-1}\left(\frac{K_\delta^2}{2 + \gamma K_\delta^2}\right)$$

where the e subscript denotes an extremum, and Λ_{be} is shown in Fig. 3. For $M_{\infty d} = 8$ and $\delta = 10$ deg, σ is 1.309 and $\Lambda_{be} = 24.3$ deg; hence, the base plane edge angle can be substantial. As with Λ_n, this is true only if δ is not too small. For instance, if $\delta = 6$ deg, then Λ_{be} is only 13.6 deg. The actual edge angle is given by

$$\Lambda_b = \Lambda_n + \omega_\Lambda(\Lambda_{be} - \Lambda_n)$$

and only depends on δ, $M_{\infty d}$, and ω_Λ, where ω_Λ is specified and ranges from 0 to 1. Thus, when $\omega_\Lambda > 0$, Λ varies smoothly from its minimum Λ_n value at the nose to its maximum value in the base plane.

With σ, Λ_b, and Ω_∞ known, Eq. (6) provides ϕ_l, which is required later. By inverting this equation, we obtain

$$\phi_l = -\Omega_\infty + \tan^{-1}\left[\frac{1 - \sqrt{1 - 4\sigma^2(\sigma^2 - 1)\tan^2\Lambda_b}}{2(\sigma^2 - 1)\tan\Lambda_b}\right] \tag{7}$$

The value for Ω_∞ is not entirely arbitrary; we constrain it by requiring that $0 \le \phi_l \le \pi/2$. This results in

$$\Omega_{\infty,\min} \le \Omega_\infty \le \Omega_{\infty,\max}$$

where

$$\Omega_{\infty,\max} = \tan^{-1}\left[\frac{1 - \sqrt{1 - 4\sigma^2(\sigma^2 - 1)\tan^2\Lambda_b}}{2(\sigma^2 - 1)\tan\Lambda_b}\right]$$

$$\Omega_{\infty,\min} = \Omega_{\infty,\max} - \frac{\pi}{2}$$

For $M_{\infty d} = 8$ and $\delta = 10$ deg, $\Omega_{\infty,\min}$ and $\Omega_{\infty,\max}$ are -33.3 and 56.7 deg, respectively. It is useful to note that these bounds depend only on δ, $M_{\infty d}$, and ω_Λ.

The thickness t (Fig. 2b) can be written nondimensionally as

$$\tau = \frac{t}{\delta l_w} = \frac{[1 + (\sigma^2 - 1)R_0^2/\sigma^2]^{1/2} - R_0}{1 - (R_0/\sigma)} \tag{8a}$$

where R_0 and l_w are shown in Fig. 1. The parameter τ, referred to as the thickness ratio, represents the normalized thickness of the waverider in the symmetry and base planes. Inversion of Eq. (8a) yields

$$R_0 = \sigma\frac{1 - \tau^2}{2\sigma\tau - (1 + \tau^2)} \tag{8b}$$

As with ϕ_l and Ω_∞, there are practical limits on R_0 and τ. The first R_0 constraint stems from the requirement that the compression surface not cross over the freestream surface. This requirement is equivalent to

$$\frac{\mathrm{d}}{\mathrm{d}Y}\left(\frac{Y}{X}\right) \ge 0, \qquad 0 < Y < Y_\sigma$$

or

$$R_0 - AY^2 - 3BY^4 \ge 0, \qquad 0 < Y < Y_\sigma$$

where A and B are given by Eqs. (4) and (5). The equality sign yields a minimum value for R_0, i.e.

$$R_{0,\min} = (\sigma/8)\cos\phi_l\{5 - 2\tan\phi_l\tan\Omega_\infty - [3(3 - \tan\phi_l\tan\Omega_\infty)(1 - \tan\phi_l\tan\Omega_\infty)]^{1/2}\}$$

where ϕ_l is given by Eq. (7). For $R_{0,\max}$, we arbitrarily set

$$R_{0,\max} = X_\sigma = \sigma\cos\phi_l$$

which corresponds to a waverider with a planar upper surface when $\Omega_\infty = 0$. With Eq. (8a), this yields

$$\tau_{\min} = \frac{-R_{0,\max}\sigma + \sqrt{R_{0,\max}^2\sigma^2 + (\sigma^2 - R_{0,\max}^2)}}{\sigma - R_{0,\max}}$$

$$\tau_{\max} = \frac{-R_{0,\min}\sigma + \sqrt{R_{0,\min}^2\sigma^2 + (\sigma^2 - R_{0,\min}^2)}}{\sigma - R_{0,\min}}$$

where

$$0 < \tau_{\min} \le \tau \le \tau_{\max} < 1$$

In parallel with Λ_b, τ is determined by

$$\tau = \tau_{\min} + \omega_\tau(\tau_{\max} - \tau_{\min})$$

where ω_τ ranges from 0 to 1. The parameter ω_τ controls the shape of the waverider in the base plane, for given values of Ω_∞ and ω_Λ. When $\omega_\tau = 0$ and $\Omega_\infty = 0$, the configuration is slender with a planar upper surface. When $\omega_\tau = 1$, it is less slender, but the freestream and compression surfaces touch for a Y where $0 < Y < Y_\sigma$.

The foregoing procedure determines the waverider configuration once δ, $M_{\infty d}$, Ω_∞, ω_Λ, and ω_τ are specified. These include its overall dimensions, i.e., length (l_w/l), span (b/l), and thickness (t/l), the latter two are in the base plane. The parameters σ, R_0, ϕ_l, A, B, . . . are still useful, since they appear in the elegant quadrature procedure[7,8] that determines geometric properties such as S_w and V, and aerodynamic properties such as the lift and drag. Equations (1), (4), (5), (7), and (8b) are utilized for determining geometric properties.

One important parameter, not previously obtained, is the ratio of the shock layer area, S_b, to the total area (between the freestream and shock curves) in the base plane. This ratio is[6]

$$\frac{S_b}{S_b + A_b} = \frac{\sigma^2 - 1}{\sigma^2} = \frac{1 + (\gamma - 1)K_\delta^2/2}{1 + (\gamma + 1)K_\delta^2/2}$$

and is shown in Fig. 3. Thus, the maximum shock layer area in the base plane that is available for a scramjet inlet is a fixed fraction of the total base area and is independent of the waverider shape. For the earlier case ($M_{\infty d} = 8$ and $\delta = 10$ deg), this fraction is 0.416.

Euler Algorithm

The Lawrence PNS space marching code[9] is used in its Euler version. Since the waverider shape is nonconical, an initial-data plane is supplied at a distance of 1% of l_w, measured from the nose. The initial data can come from HSDT, for on-design operation, or a time-marching Euler code for both on- and off-design operation. The space-marching code is used because of its computational efficiency. A detailed comparison of solutions in the base plane verified the accuracy of

this approach.[6] The grid generation technique used was developed by Thompson.[10] Grid lines are obtained by solving Poisson's equation with source terms as control functions. The grid for an inviscid calculation of a sharp-edged waverider with the space-marching code is 64 × 41 and 67 × 41 for a rounded leading edge.

Leading-Edge Rounding

The first investigation[11] of edge rounding experimentally showed that the pressure is affected only close to the leading edge. More recently, Refs. 2 and 4 have computationally reexamined this topic. In particular, Ref. 4 used a circular arc to round the edge whose radius appreciably increased with downstream distance. As in Ref. 11, pressure changes occur only close to the leading edge, a result our calculations reconfirm. More importantly, Vanmol and Anderson[4] point out that the nature of the boundary layer on the freestream and compression surfaces is affected by rounding, particulary by the induced crossflow velocity. Thus, rounding can have an important effect on both skin friction and heat transfer.

Since we desire a smooth, as well as flexible, curve to replace the sharp edge, a third-order continuous B-spline curve is used.[6] As a consequence, the surface has both continuous first derivatives and continuous curvatures. (A discontinuous curvature in a supersonic flow may lead to boundary-layer separation.) In order that the variation of the radius of curvature normal to the edge be approximately uniform, the rounding near the nose is about 3% of the local span, while only 1% of the span in the base plane. A highly expanded view of the grid at a rounded edge is shown in Fig. 4.

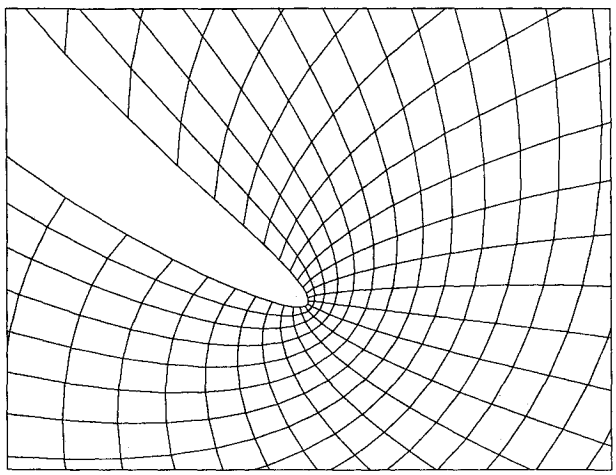

Fig. 4 Computational grid near a rounded leading edge.

Results

We consider waverider forebodies with a 20-m length that are flying at a 24-km altitude. The corresponding Reynolds number, $(\rho V l_w/\mu)_\infty$, is 1.55×10^8. On-design results, based on HSDT, are first presented.

On-Design Results

Table 1 summarizes the parametric analysis, where the first five rows are input, the next six rows show geometric output, while the last six rows contain lift and drag values. Laminar results in this last group are based on the theory in Ref. 8, and are meant to provide trends. (Nevertheless, the boundary layer on a free-flight 10-deg cone at $M_\infty = 3$ was still laminar at the largest Reynolds number, 5×10^7, of the experiment.[12])

Configuration 1 in Table 1 is a nominal case; several views of it are shown in Fig. 5. This configuration is not an optimum one, either in terms of η or L/D. Other configurations, i.e., number 4, have larger η and L/D values. Configuration 1, however, is typical of the nonslender shapes generated with this approach. Noteworthy points are the sizable edge angle Λ_b (=24.3 deg), the sizable volumetric parameter (=0.239), and the small difference between the inviscid and viscous L/D values. Observe the relatively small ϕ_l value, which is characteristic of this class of waverider shapes.

Trends for L/D, η, and ϕ_l are shown in Figs. 6–8 in which $M_{\infty d} = 8$, $\delta = 10$ deg, and the nonvarying parameters have their nominal value. Large L/D and η values (see Fig. 6) favor Ω_∞ values around 30–40 deg, and a relatively small ϕ_l. The sharp drop in L/D occurs when $\Omega_\infty \to \Omega_{\infty,\max}$, in which case $\eta \to \infty$, $\phi_l \to 0$, and the waverider degenerates to a vertically oriented plate. While a conventional slender waverider has an η, typically in the range 0.12–0.19, the other slender waverider extreme has $\eta > 0.3$. Thus, nonslender waveriders should have an intermediate η value. Observe that once Ω_∞ is well below $\Omega_{\infty,\max}$, both L/D and η are insensitive to it.

Figure 7 shows variations with respect to ω_τ. Although the shape of a waverider in the base plane depends on ω_τ, as will be discussed, neither L/D or η are sensitive to it. The reason for this is that τ is normalized with δ, and it is L/D and η that are strongly δ dependent. Figure 8 shows a similar plot with ω_Λ as the independent parameter. A value for ω_Λ near 0.7 is favored. The zero values for ϕ_l and L/D when $\omega_\Lambda = 0.54$ occur because ϕ_l is ω_Λ dependent, as evident in Eq. (7). Note that ϕ_l does not depend on ω_τ; hence, the relatively flat curves in Fig. 7. Moreover, when ϕ_l is not too small, Figs. 7 and 8 show that ω_τ and ω_Λ have little effect on L/D. Thus, for a

Table 1 Properties of HSDT waveriders

Configurations	1	2	3	4	5	6	7	8	9	10	11	12	13
$M_{\infty d}$	8	8	8	8	8	8	8	8	8	8	8	8	4
δ	10	6	10	10	10	10	10	10	10	10	10	10	15
Ω_∞	30	−40.4	0	10	20	0	10	20	30	20	40	30	30
ω_Λ	1	0	0.5	0.5	0.5	0.5	0.5	0.5	1	1	1	1	1
ω_τ	0.7	0.3	0.5	0.5	0.5	0.9	0.9	0.9	0.5	0.7	0.7	0.9	0.7
Λ_b	24.3	3.63	15.9	15.9	15.9	15.9	15.9	15.9	24.3	24.3	24.3	24.3	18.1
τ	0.888	0.763	0.860	0.851	0.847	0.920	0.914	0.911	0.858	0.898	0.881	0.918	0.883
ϕ_l	27.2	50.0	28.8	18.8	8.8	28.8	18.8	8.8	27.2	37.2	17.2	27.2	24.0
b/l_w	0.344	0.490	0.449	0.325	0.162	0.303	0.209	0.101	0.432	0.428	0.232	0.289	0.509
S_w/S_p	2.49	2.08	2.29	2.67	4.24	2.72	3.47	6.19	2.28	2.25	3.18	2.73	2.72
η	0.239	0.136	0.220	0.244	0.308	0.253	0.285	0.362	0.220	0.225	0.271	0.255	0.256
$C_L \times 10$	0.668	0.249	0.657	0.654	0.652	0.678	0.677	0.676	0.657	0.671	0.666	0.678	1.55
$C_{D\text{inv}} \times 10^2$	0.921	0.174	0.902	0.884	0.874	0.940	0.922	0.911	0.902	0.949	0.902	0.939	2.88
$(L/D)_{\text{inv}}$	7.26	14.3	7.28	7.39	7.46	7.21	7.34	7.42	7.28	7.07	7.38	7.22	5.38
$C_f \times 10^3$	0.137	0.136	0.136	0.137	0.140	0.138	0.140	0.141	0.134	0.135	0.139	0.138	0.194
$C_D \times 10^2$	0.955	0.203	0.933	0.921	0.933	0.978	0.970	0.998	0.932	0.979	0.946	0.977	2.93
L/D	7.00	12.3	7.04	7.10	6.98	6.93	6.98	6.77	7.04	6.85	7.04	6.94	5.28

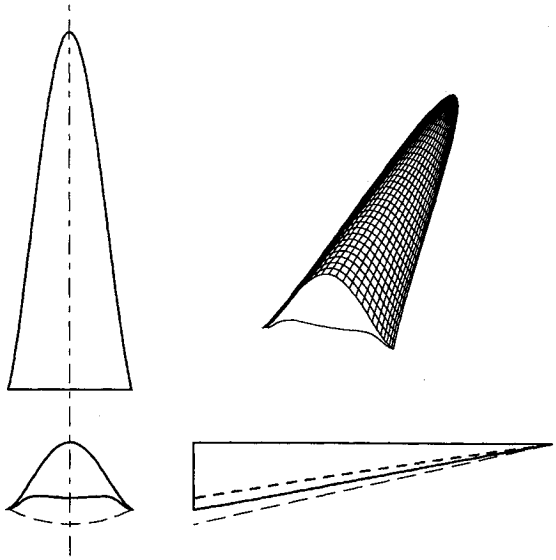

Fig. 5 Scaled views of configuration 1.

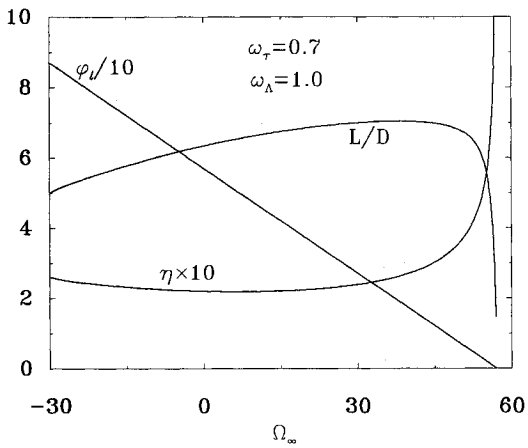

Fig. 6 Variation of ϕ_l, L/D, and η vs Ω_∞.

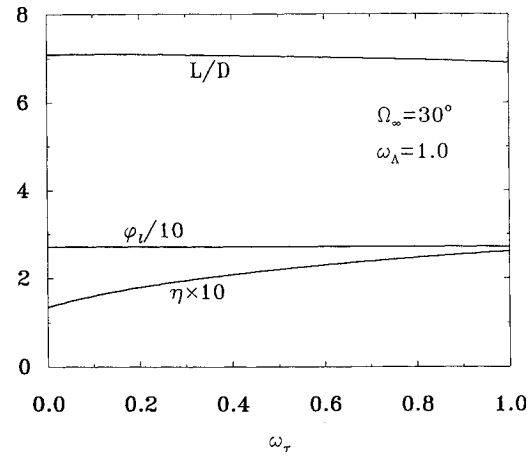

Fig. 7 Variation of ϕ_l, L/D, and η vs ω_τ.

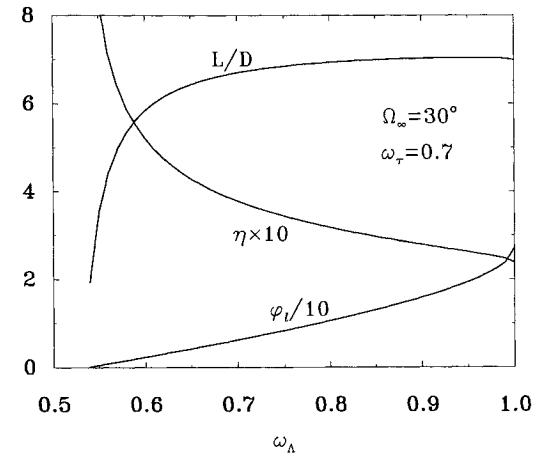

Fig. 8 Variation of ϕ_l, L/D, and η vs ω_Λ.

given δ value, it is possible to have a large included edge angle and a favorable volumetric distribution without an undue loss in L/D.

Configuration 2 is a typical slender waverider; its base plane shape is shown in Fig. 9. While its L/D is larger than that of configuration 1, its viscous drag increment is also larger. The increase in the drag coefficient caused by the boundary layer is only 3.7% for configuration 1, but is 16.7% for configuration 2. This difference increases rapidly with decreasing Reynolds number. Thus, the difference in viscous L/D between slender and nonslender waveriders narrows for either a reduced vehicle length or a higher flight altitude. In addition, configuration 2 has a small η value and an edge angle Λ_b of only 3.6 deg.

Except for configuration 2, all the cases in Table 1 have τ close to 0.9. The importance of τ is illustrated in Fig. 9 by comparing configuration 2 to the other cases. (All six views are to scale for the same l_w.) Although configuration 2 has a large shock layer area fraction $S_b/(S_b + A_b)$ (=0.619) compared to configuration 1 (and 3–12), its spread-out shock layer is less suitable for a scramjet inlet from a structural viewpoint. The ϕ_l value of 50 deg (configuration 2) is a typical slender waverider value. Figures 6 and 8, however, show that a smaller ϕ_l value provides a maximum L/D as well as a more compact scramjet inlet.

While configurations 1 and 4 differ in Ω_∞, ω_Λ, and ω_τ; the base plane shapes are similar, as are the L/D and η values. The principal difference arises in the value of Λ_b, with configuration 4 having a smaller value. Configurations 10–12 in Fig. 9 illustrate the effect of Ω_∞ and ω_τ. Inserts in the figure show enlarged leading-edge views for two configurations. Note the very sharp edge of configuration 2. Even a small amount of rounding would remove a significant portion of the structure, with a large adverse impact on L/D as compared to a less sharp-edged waverider. In its full view, configuration 11 appears to have a sharp-edged winglet, however, the insert shows this not to be the case, since Λ_b = 24.3 deg.

The narrow span of configuration 11 is evident from its S_w/S_p value of 3.18 and ϕ_l, which is only 17.2 deg. Narrow waveriders are characterized by large values for η and S_w/S_p, and small values for ϕ_l and the aspect ratio b/l_w. Configurations 5, 7, and 8 are in this category. The L/D of these configurations is less than most of the others because of their larger wetted surface area, and therefore, increased viscous drag.

Configuration 13 is for $M_{\infty d}$ = 4 and δ = 15 deg (Table 1 and Fig. 9). Its geometric properties are similar to some of the $M_{\infty d}$ = 8 configurations, while its L/D has decreased to 5.28. Its large Λ_b value and base area A_b stem from the large δ value. The other lift and drag parameters for this configuration in Table 1 are larger because of the $M^2_{\infty d}$ normalization. In this regard, C_L, C_D, and C_f are normalized with the planform area.

The lower L/D value at $M_{\infty d}$ = 4 is typical of both slender and nonslender waveriders. This value would significantly increase if a smaller δ value is chosen.[6] However, a smaller value for δ results in a sharp reduction in both η and Λ. As a consequence of this tradeoff, it appears that the nonslender

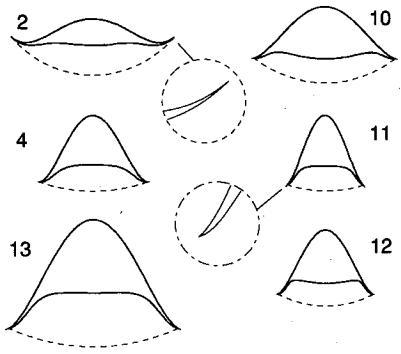

Fig. 9 Base plane views of selected waveriders from Table 1, where numbers denote the configuration.

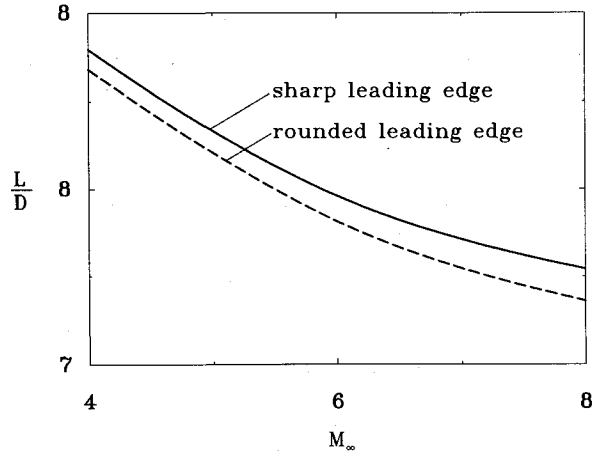

Fig. 10 *L/D* at off-design Mach numbers for configuration 1 with $\alpha = 0$, and with sharp and rounded leading edges.

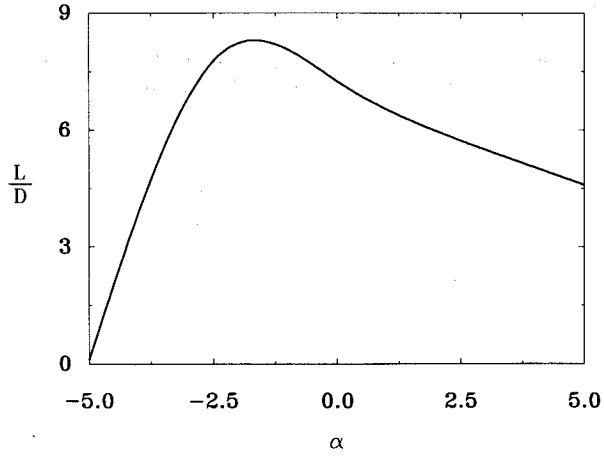

Fig. 11 *L/D* vs α for configuration 1 when $M_{\infty d} = 8.3$.

approach may be most viable for hypersonic design Mach numbers in the medium-to-high range.

Off-Design Results

The CFD calculations are only performed for the configuration 1 nominal case. Even though the shock appears to be attached to the leading edge at $M_\infty = 8$, there remains a small disturbance on the freestream surface near the edge. This is caused by the HSDT shapes, which are only approximate. This disturbance disappears when $M_\infty = 8.3$, and this Mach number is regarded as the on-design value for this waverider shape. The off-design Mach numbers range from 4 to 8.3,

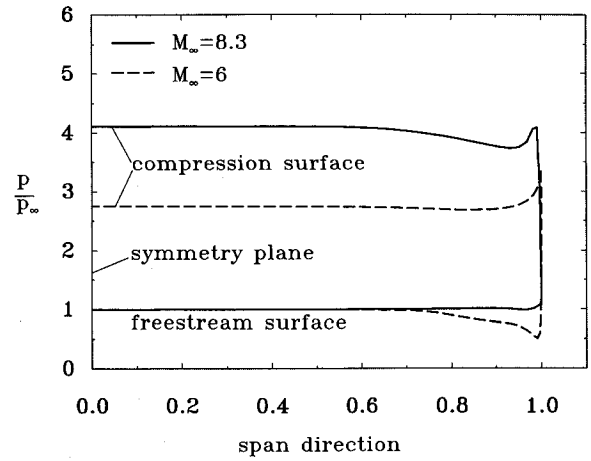

Fig. 12 Pressure distribution in the base plane at $M_\infty = 6$ and 8.3 for configuration 1 with sharp leading edge at $\alpha = 0$.

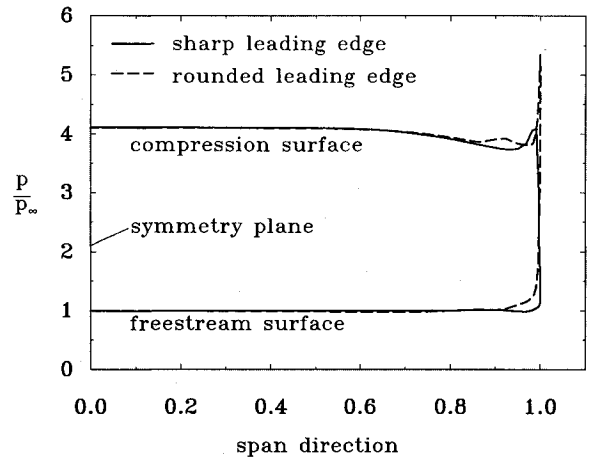

Fig. 13 Pressure distribution in the base plane at $M_\infty = 8.3$ for configuration 1 with sharp and rounded leading edges at $\alpha = 0$.

while the angles of attack, at $M_\infty = 8.3$, range from -5 to $+5$ deg.

Figure 10 shows *L/D* as a function of M_∞ at zero angle of attack. At Mach numbers lower than the on-design value, *L/D* increases as M_∞ decreases. Figure 11 shows *L/D* vs α with a maximum *L/D* occurring at -1.9 deg. The zero *L/D* value occurs near -5 deg, which is approximately $\alpha = -\delta/2$. Figure 12 shows the pressure distribution in the base plane for $M_\infty = 6$ and 8.3. When $M_\infty < M_{\infty d}$, a low-pressure region develops on the freestream surface and a high-pressure region is on the compression surface, with both regions near the leading edge. These regions contribute to a higher *L/D* when $M_\infty < M_{\infty d}$. The large pressure gradient at the leading edge requires a smaller marching step in the Euler calculations. The *L/D* trends, however, are similar for slender and nonslender waveriders with aerodynamic properties slightly less sensitive at off-design conditions for a nonslender waverider.[6]

Waverider results with a rounded edge are shown in Figs. 10 and 13. The rounded edge *L/D* is only a few percent less compared to the *L/D* for a sharp leading edge. This suggests that rounding has only a local effect, and the nature of the inviscid flowfield around the waverider is unchanged. The pressure distribution in the base plane when $M_\infty = 8.3$ shows this limited effect, with a pressure increase only in a small region near the leading edge.

Concluding Remarks

An analytical/computational study is presented of the geometric and aerodynamic properties of waveriders. To enhance

their application, several features are discussed: increase the body's thickness, especially in the base plane, increase the included angle at the leading edge, and uniformly round the leading edge. These changes come at the price of a reduced lift-to-drag ratio. Nevertheless, the L/D is still large, particularly if the waverider is designed for flight at a substantial Mach number. On-design configurations are examined, primarily at $M_{\infty d} = 8$, using hypersonic small-disturbance theory. A body-oriented design procedure is developed along with constraints. A Euler code is used to examine off-design performance caused by a reduction in the flight Mach number, angle of attack, and leading-edge rounding. Leading-edge rounding causes a small reduction in L/D, while a variation in the angle of attack results in comparable performance to slender waveriders. When $M_\infty < M_{\infty d}$, the bow shock stands off from the vehicle's surface, i.e., there is no shock wave boundary-layer interaction, and the L/D is increased from its design value. Thus, there are important benefits to be obtained by designing the waverider at its highest anticipated flight Mach number when in endoatmospheric flight.

Acknowledgment

The authors gratefully acknowledge the comments of M. L. Rasmussen.

References

[1]Anderson, J. D., Jr., Ferguson, F., and Lewis, M. J., "Hypersonic Waveriders for High Altitude Applications," AIAA Paper 91-0530, Jan. 1991.

[2]Jones, K. D., Bauer, S. X. S., and Dougherty, F. C., "Hypersonic Waverider Analysis: A Comparison of Numerical and Experimental Results," AIAA Paper 91-1696, June 1991.

[3]Center, K. B., Sobieczky, H., and Dougherty, F. C., "Interactive Design of Hypersonic Waveriders Geometries," AIAA Paper 91-1697, June 1991.

[4]Vanmol, D. O., and Anderson, J. D., Jr., "Heat Transfer Characteristics of Hypersonic Waveriders with an Emphasis on Leading Edge Effects," AIAA Paper 92-2920, July 1992.

[5]Liao, J. R., Isaac, K. M., Miles, J. B., and Tsai, B.-J., "Navier-Stokes Simulation for Cone-Derived Waverider," *AIAA Journal*, Vol. 30, No. 6, 1992, pp. 152–158.

[6]He, X., "Computational Analysis of Hypersonic Flows Past Generalized Cone-Derived Waveriders," Ph.D. Dissertation, School of Aerospace and Mechanical Engineering, Univ. of Oklahoma, Norman, OK, 1992.

[7]Rasmussen, M. L., and Stevens, D. R., "On Waverider Shapes Applied to Aerospace-Plane Forebody Configurations," AIAA Paper 87-2550, Aug. 1987.

[8]Rasmussen, M. L., and He, X., "Analysis of Cone-Derived Waveriders by Hypersonic Small-Disturbance Theory," *Proceedings of the First International Waverider Symposium*, Univ. of Maryland, College Park, MD, Oct. 1990.

[9]Lawrence, S. L., Tannehill, J. C., and Chaussee, D. S., "An Upwind Algorithm for the Parabolized Navier-Stokes Equations," AIAA Paper 86-1117, May 1986.

[10]Thompson, J. F., Thames, F. C., and Mastin, C. W., "Boundary-Fitted Curvilinear Coordinate Systems for Solution of Partial Differential Equations on Fields Containing Any Number of Arbitrary Two-Dimensional Bodies," NASA CR-2729, July 1977.

[11]Pike, J., "Experimental Results from Three Cone-Flow Waveriders," *Hypersonic Boundary Layer and Flow Fields*, AGARD Conf. Proc. 30, May 1968.

[12]Sternberg, J., "A Free-Flight Investigation of the Possibility of High Reynolds Number Supersonic Laminar Boundary Layers," *Journal of Aeronautical Sciences*, Vol. 19, Nov. 1952, pp. 721–733.

Best Seller!

Recommended Reading from
Progress in Astronautics and Aeronautics

Test and Evaluation of the Tactical Missile

E.J. Eichblatt, Jr., D.B. Meeker, P.B. McQuaide, K.W. Canaga, and A. Pignataro

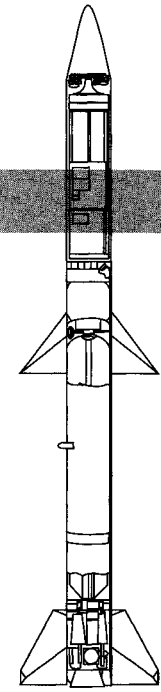

More than a quarter-century of experience document the trends and technologies reported in this volume. Now others in the field have the means to determine whether a missile meets its requirements, functions operationally, and should continue on into production, before a program's time and costs are scheduled, or a system is acquired.

Topics include: missile performance; flight test; laboratory/field test; simulation; launchers; T&E of insensitive munitions; reliability T&E; electromagnetic environment effects (E3) testing and more.

1989, 432 pp, illus, Hardback, ISBN 0-930403-56-8
AIAA Members $54.95, Nonmembers $65.95
Order #: V-119 (830)

Place your order today! Call 1-800/682-AIAA

AIAA
American Institute of Aeronautics and Astronautics

Publications Customer Service, 9 Jay Gould Ct., P.O. Box 753, Waldorf, MD 20604
FAX 301/843-0159 Phone 1-800/682-2422 9 a.m. - 5 p.m. Eastern

Sales Tax: CA residents, 8.25%; DC, 6%. For shipping and handling add $4.75 for 1-4 books (call for rates for higher quantities). Orders under $100.00 must be prepaid. Foreign orders must be prepaid and include a $20.00 postal surcharge. Please allow 4 weeks for delivery. Prices are subject to change without notice. Returns will be accepted within 30 days. Non-U.S. residents are responsible for payment of any taxes required by their government.